Experimental and numerical investigation of cavitation-induced erosion in thermal sprayed single splats

Yan WANG[1,2✉], Bruno LEBON[3], Iakovos TZANAKIS[4,5], Yongli ZHAO[2], Kuaishe WANG[1], Jorge STELLA[6], Thierry POIRIER[7], Geoffrey DARUT[2], Hanlin LIAO[2], Marie-Pierre PLANCHE[2]

[1] School of Metallurgical Engineering, Xi'an University of Architecture and Technology, Xi'an 710055, China

[2] Univ. Bourgogne Franche-Comté, ICB UMR 6303, CNRS, UTBM, 90010 Belfort, France

[3] Brunel University London, Brunel Centre for Advanced Solidification Technology, Uxbridge, United Kingdom

[4] Oxford Brookes University, School of Engineering, Computing and Mathematics, Oxford, United Kingdom

[5] University of Oxford, Department of Materials, Oxford, OX1 3PH, United Kingdom

[6] Universidad Simón Bolívar, Departamento de Ciencia de los Materiales, Caracas, Venezuela

[7] Institut de Céramique Française, Limoges France

✉Corresponding author, wangyan140511@hotmail.com

Abstract

Hydraulic components are coated by thermal spraying to protect them against cavitation erosion. These coatings are built up by successive deposition of single splats. The behavior of a single splat under mechanical loading is still very vaguely understood. Yttria-stabilized zirconia (YSZ) and stainless-steel splats were obtained by plasma spraying onto stainless steel substrates. The velocity and temperature of particles upon impact were measured and the samples were subsequently exposed to cavitation erosion tests. An acoustic cavitation simulation estimated the water jet velocity and hammer stresses exerted by bubble collapse on the surface of the specimen.

Although the results suggested that high stress levels resulted from cavitation loading, it was clear that weak adhesion interfaces played a crucial role in the accelerated cavitation-induced degradation.

Keywords: cavitation erosion, plasma spraying, single splat, numerical modelling, adhesion, cohesion

1. Introduction

Hydraulic machinery such as valves, propellers, impellers, pumps and turbines [1–4] suffers from severe cavitation erosion, causing life shortening and maintenance problems. Cavitation erosion is a surface degradation process caused by the repeated collapse of cavitation (vapor/gas) bubbles. Collapsing cavities induce shock waves and liquid impinging on the adjacent surface [5], increasing the local pressure up to 1 GPa [6]. This process repeats thousands times a second [7] resulting in material fatigue and considerable mass removal up to 200 kg in large-scale components (such as hydraulic turbines) after serving for a few years [8]. As a consequence, material removal from the surface leads to poor performance of the components. Although significant efforts have been made to minimize cavitation erosion by improving the design of hydraulic plants [9], in practice cavitation erosion cannot be avoided [10].

Generally, materials with high cavitation erosion resistance are chosen as the building materials of hydro machinery. Martensitic stainless steels are among them because of their corrosion resistance, acceptable resistance against cavitation erosion, moderate cost, and welding suitability [4, 11]. Moreover, surface engineering is usually used to further improve the cavitation resistance of hydro plants. Welding and thermal spraying are the most commonly used surface techniques to coat a protective layer on the metallic surface for protection against cavitation erosion.

Welding is often used to repair cavitation erosion damage. The affected area is first removed then welded with martensitic stainless steel fillers [12]. However, surface preparation of the eroded (hydraulic) profiles after welding is time-consuming. In addition, extensive welding results in large heat input and can damage the base metal [13]. Therefore, applying a wear resistant layer by thermal spraying has attracted increasing attention as a means of protection against cavitation erosion. Hard-facing materials such as Stellite 6, Tribology T-400 [13] and WC-Co [14] have been used as thermally sprayed protective coatings due to high hardness and corrosion resistance. In addition, thermally sprayed NiTi coatings exhibit an excellent performance against cavitation erosion due to their reversible stress-induced martensitic phase transformation [1,15,16]. YSZ Ceramic material is also considered as interesting candidates for resisting cavitation based on stress-induced tetragonal-monoclinic martensitic transformation under cavitation conditions [17]. However, the cavitation properties of YSZ degrade when they are thermally sprayed.

The failure mechanism of plasma sprayed YSZ coatings has been discussed by Wang *et al*. [18]. According to this study, the initial defects inside the as-sprayed coatings such as cracks, pores, splashes and incomplete contact interfaces contribute to the early damage of YSZ coating under cavitation impact. A thermal spray coating is built by the successive deposition of droplets. Different splats stages (molten or half molten) lead to quite different coating microstructures and properties [19]. For example, thermal spraying of completely molten YSZ particles (generally disk-shaped splats) results in an improved microstructure of the coating with well-adhered splats, decreased porosity, higher thermal conductivity and elastic modulus [20]. Therefore, it is essential to understand the cavitation erosion behaviour of a single splat in order to study the cavitation erosion of a thermal sprayed coating. In the present study, 8 wt% YSZ and 304 stainless steel (304SS) single splats were plasma sprayed onto stainless steel substrates. To investigate the mechanical behaviour of cavitation-induced erosion in a thermal sprayed single

splat, the samples were subjected to cavitation in water. The stresses exerted by bubble collapse were numerically investigated.

2. Methodology

2.1. Coatings preparations and characterizations

YSZ (Saint Gobain, France) and 304 SS (LTS Research Laboratories, USA) powders were plasma sprayed on 304 stainless steel substrates. Their size distributions were determined by laser diffraction (Mastersizer 2000, Malvern, England). An average size of 26.8 µm was found for YSZ with D_{10} = 15.7 µm, D_{50} = 25.3 µm and D_{90} = 40.3 µm. The D_{10}, D_{50} and D_{90} labels represent that the volumetric percentage of particles with diameter less than the stated diameter in the subscript. For example, D_{10} = 15.7 µm means that 10% of the total volume of particles have a diameter smaller than 15.7 µm. The average size of 304SS is 38.1 µm and D_{10}, D_{50} and D_{90} are 19.4 µm, 35.3 µm and 61.1 µm respectively (**Figure 1**). Materials properties of YSZ and 304SS are presented in **Table 1**.

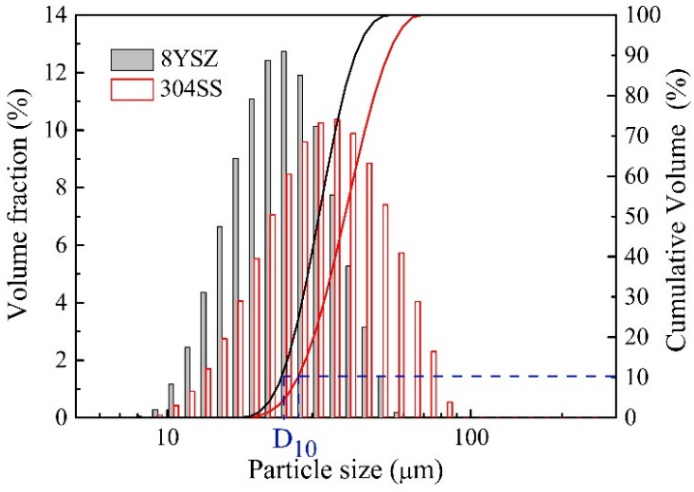

Figure 1: Size distribution of the powders

Table 1: Material properties of YSZ and 304SS

Properties	Density ($g\ cm^{-3}$)	Melting point (°C)	0.2% Yield stress (MPa)	Thermal conductivity ($W\ m^{-1}\ K^{-1}$)	Young's modulus (GPa)	Poisson's ratio
YSZ	~6.1	2800	-	~1.5	40_50	0.22
304SS	8.03	~1400	290	~13	190_200	0.29

Single splats deposition was carried out employing a Sulzer-Metco F4 plasma gun. The experimental set-up of plasma spraying is shown in **Figure 2**. **Table 2** shows the spray conditions. The parameters were chosen based on previous experiments [18]. The substrates were mirror polished and preheated to 180 °C before deposition and placed upon a rotating table (500 rpm, corresponding to a liner spraying velocity of 5 $m\ s^{-1}$), in order to get single deposition splats.

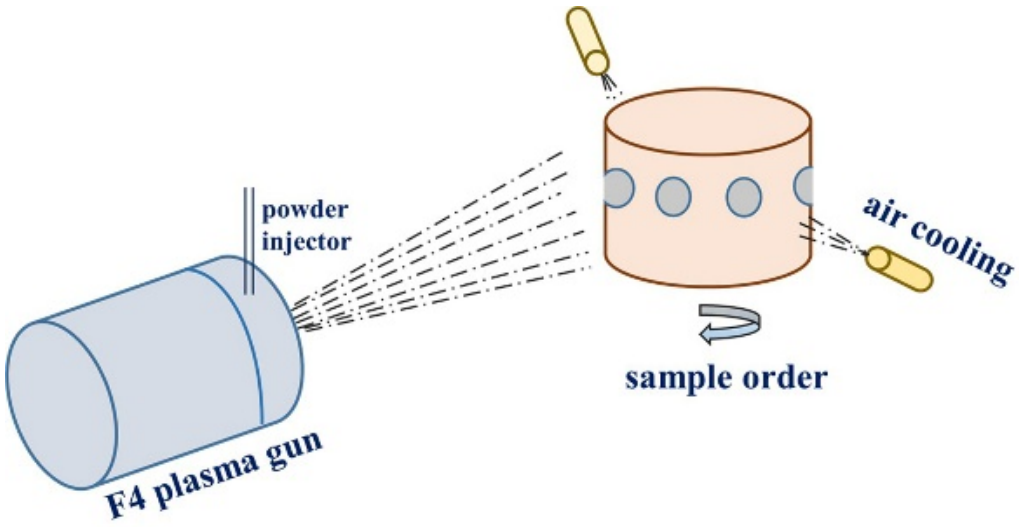

Figure 2: Schematic of experimental set-up on plasma spraying

Table 2: Spray conditions

Parameters	YSZ	304SS
Electric arc current (A)	620	600
Electric arc voltage (V)	60	56
Plasma gas (SLPM*) Ar	35	50
Plasma gas (SLPM) H_2	11	6
Carrier gas (SLPM)	1.8	2.2
Liner speed (m s^{-1})	5	5
Stand-off distance (mm)	110	125

*SLPM: standard liter per minute

A DPV 2000 sensor measured in-flight temperature, velocity and size of particles upon impact (Tecnar automation Ltee, St-Bruno, Canada). The sensing head is located in the spray plume. A 785 nm laser is used to radiate the particles passing the optical sensor. The measurement of velocity and temperatures is based on the analysis of the reflected light [21]. More than 2000 particles were detected to calculate the average values. Scanning Electron Microscopy (JEOL, JSM-5800LV, Japan) was used to characterize the morphology of initial powders and microstructures of the single splats (with and without cavitation erosion).

2.2. Cavitation erosion tests

Cavitation erosion tests were conducted according to the main guidance of ASTM G32 with a frequency adjusted to 20 kHz maintaining a peak-to-peak amplitude of 45 μm for 2 min. A stepped titanium sonotrode with 13 mm (VC300, Sonics, USA) diameter tip immersed 12 mm in the water below the free surface introduced vibrations in the liquid medium. The set-off distance between the sonotrode tip and undergoing coating was 0.5 mm (**Figure 3**). Steel samples were

mounted on the bottom of a transparent tank with diameter of 60 mm filled with 2 L of distilled water. Cavitation created by the small horn generated a gradual damage that was useful for studying the mechanisms of cavitation erosion, while the energy released by cavitation did not significantly affect the water temperature that was maintained at 22 ±1 °C.

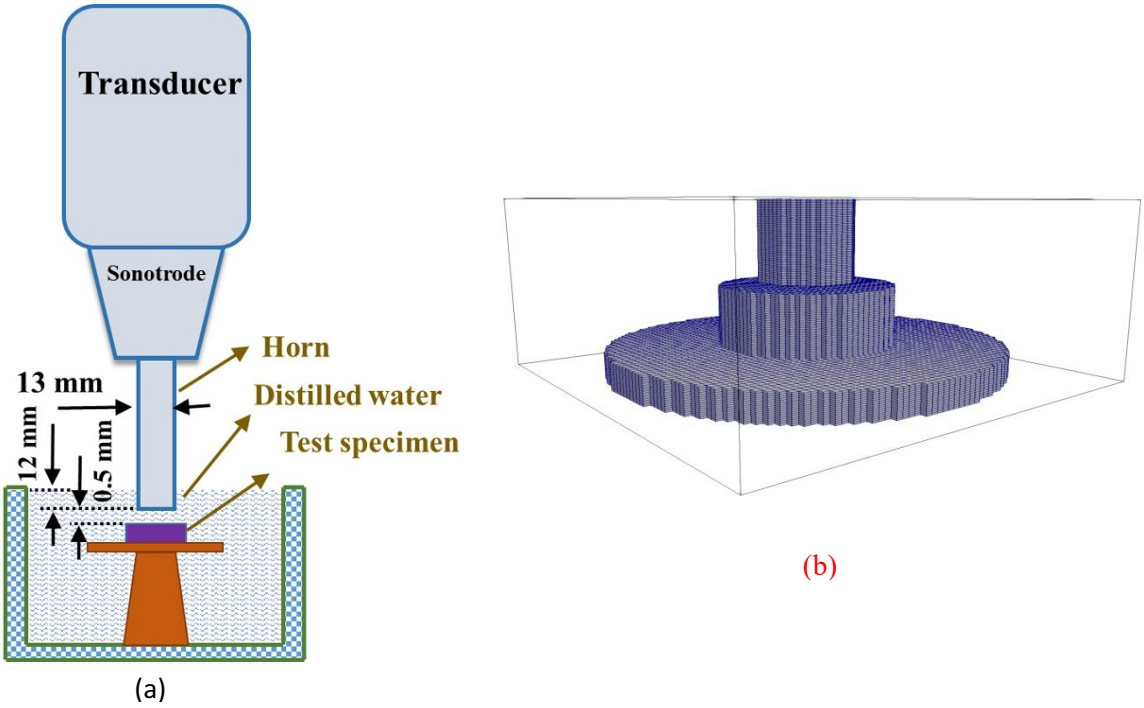

Figure 3: (a) Cavitation erosion test device (b) Castellated mesh of horn, test specimen, and supporting stand in the computational domain

2.3. Numerical analysis

The pressure exerted by bubble collapse on the surface of the specimen was evaluated using Lebon's *et al.* numerical model of acoustic cavitation [22]. Coupled equations of mass conservation, momentum conservation, and bubble dynamics are solved for using a high-order finite difference method for the partial differential equations and an explicit version of the 4th Merson method for the ordinary differential equation:

$$\frac{\partial p}{\partial t} + v_j \frac{\partial p}{\partial x_j} + \rho c^2 \frac{\partial v_j}{\partial x_j} = \rho c^2 \frac{\partial \phi}{\partial t} \quad (1)$$

$$\frac{\partial v_i}{\partial t} + v_j \frac{\partial v_i}{\partial x_j} + \frac{1}{\rho}\frac{\partial p}{\partial x_i} = \frac{\partial \tau_{ij}}{\partial x_j} + F_i \quad (2)$$

$$R\ddot{R} + \frac{3}{2}\dot{R} = \frac{p_s}{\rho} \quad (3)$$

where p is the acoustic pressure, v_j are the velocity components, ρ is the (pure) liquid density, and $c \equiv \sqrt{\partial p/\partial \rho}$ is the speed of sound in the liquid. $\phi = \frac{4}{3}\pi n_0 R^3$ is the bubble phase fraction, where n_0 is the number of bubbles, each of radius R, per unit volume. The acoustic velocity sources are prescribed in the momentum source term F_i. $\frac{\partial \tau_{ij}}{\partial x_j}$ accounts for acoustic energy dissipation due to viscosity. $p_s = p_b(t) + p_v - \frac{2\sigma}{R} - \frac{4\mu\dot{R}}{R} - p(t)$. $p_b = p_{g,0}\left(\frac{R_0}{R}\right)^{3\kappa}$ is the pressure inside the bubble, with $p_{g,0}$ being the gas pressure at the equilibrium radius R_0. $\kappa = 0.14$ is the polytropic exponent. p_v is the bubble vapour pressure. σ is the surface tension between the liquid and the bubble gas. μ is the dynamic viscosity of the liquid.

A 3D model was run based on the experimental setup (**Figure 3**) allowing a complete representation of the impact pressures acting on the surface. Detailed information of pressure solver can be found elsewhere [22,23]. In summary, the equations governing sound propagation are coupled with a model representing the dynamics of individual bubbles. The initial pressure and velocity components in the liquid are set to zero. The liquid is assumed to contain 10^{11} bubbles per m^3, each of the average radius 10 μm. All solid surfaces are assumed perfectly reflective to sound waves. The free surface is approximated by fixing pressures above the water level to 0 Pa. The solution to these equations requires a high-order discretization method that minimizes numerical dispersion. In our implementation, a castellated uniform mesh of the

geometry illustrated in **Figure 3** is used as the discretization method requires a uniform grid in each coordinate direction. The domain below the stand was truncated and a transparent boundary condition was used at the bottom of the computational domain.

The collapsing bubble velocity jet v_{jet} is estimated taking into account the bubble asymmetry adjacent to a solid surface [24,25] using equation (4)

$$v_{jet} = 4.6\sqrt{\frac{p-p_v}{\rho_l}} \tag{4}$$

Maximum erosion damage due to velocity jets occurs when the initial distance from the surface is around 0.75 of the bubble radius.

The pressure p is obtained by solving the wave equation in bubbly media as described in [21, 22] where p_v and ρ_l are the vapour pressure and density of water, respectively.

This jet velocity is used as a parameter in equation (2), which is based on the physical description of collapsing of the cavitating bubble cloud in order to predict the velocity and local pressure [26]

The water hammer stress applied on the specimen surface (p_{hammer}) is estimated as:

$$p_{hammer} \approx 0.6 v_{jet} \rho_l c_l \tag{5}$$

where c_l is velocity of sound in pure water.

Deformation occurs when p_{hammer} is larger than a critical pressure above which plastic flow of the material occurs. Therefore, to reach the yield stress of the material, a critical velocity (v_{crit}) has to be reached [27].

$$v_{crit} = \sqrt{\frac{p_y}{\rho_l}\left(1 - \left(1 + \frac{p_y}{B}\right)^{-\frac{1}{n}}\right)} \tag{6}$$

where p_y represents the yield stress of material, B=300 MPa and n=7

$$p_{def} \approx v_{def}\rho_l c_l = \left(0.6 v_{jet} - v_{crit}\right)\rho_l c_l \tag{7}$$

where p_{def} and v_{def} are the deformation pressure and the deformation velocity, respectively.

3. Results

3.1. In-flight particle temperature and velocity

Measurements of the in-flight particle temperature and velocity are shown in **Figure 4**. The abscissa corresponds to the vertical positions at off-set distance. The temperatures of 304SS particles are 2230_2390 °C, with a standard deviation around 100 °C. The temperature of 304SS particles is seemingly less dependent on the detected position. The temperature is above the melting point of 304SS (~ 1400 °C). The highest velocity detected is 218 ± 9 m s^{-1}. It varies from 170 m s^{-1} to 218 m s^{-1} in different positions. For YSZ particles, plasma spraying leads to a velocity of 280 ± 20 m s^{-1} and a temperature value of 2880 ± 80 °C for the smallest particle with an average size of 25.3 μm and a velocity of 176 ± 15 m s^{-1} and a temperature value of 2550 ± 99 °C for the largest particle with an average size of 30.6 μm. The melting point of the YSZ particles is around 2700 °C meaning that the in-flight YSZ particles consist of some un-melted and half-melted particles. Both temperature and velocity values of YSZ particle are higher than those of 304SS particle in the same detected position. Generally, the velocity of particles decreases with an increase in diameter during the plasma spraying process because of the higher inertia of larger particles. In this study, the 304SS particles have a larger size than that of the YSZ (**Figure 1**) along with a higher density (304SS ~ 8.03 g cm^{-3}) > (YSZ ~ 6.1 g cm^{-3}). Moreover, the maximum temperature of an argon-hydrogen plasma jet is normally reached at the end of the plasma core, which is almost 50 mm downstream of the nozzle exit [28]. Thus, the particles begin to decelerate and cool down during the following step of flight. However, the thermal

conductivity (~1.5 W m^{-1} K^{-1}) of YSZ particle is lower than that of 304SS (~13 W m^{-1} K^{-1}) resulting in a higher temperature of YSZ particles (Table 1).

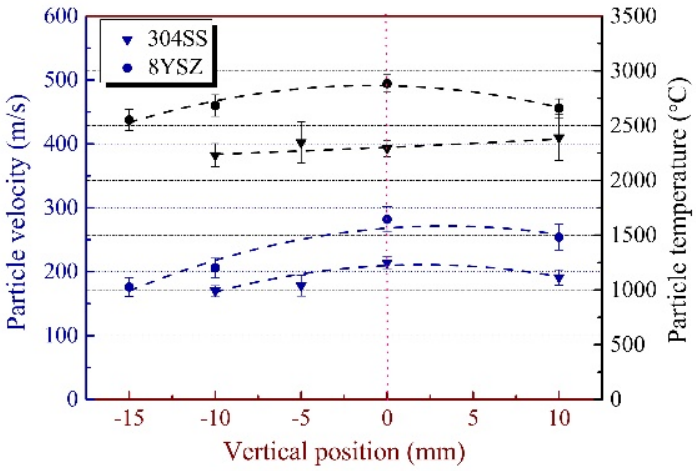

Figure 4: Velocity and temperature of impinging particles

3.2. Cavitation erosion

Both initial YSZ and 304SS single splats are observed with disk-shaped (**Figure 5a** and **c**) patterns. Only few short ejections of materials were found near the periphery of the 304SS and YSZ splats (indicated by yellow arrow in **Figure 5c**). They are usually observed during splat impact (occurring in few microseconds). These ejections lead to the poor adhesion of the splat to the substrate. The ejections are removed firstly after 2 min cavitation erosion (Figure 5.b and d). Unfortunately, it is still not understood how and when they are generated during splat formation. Crack networks on the YSZ splats are formed because of the relaxation of the quenching stresses along with the brittle behavior of YSZ. Some wave-like morphology (indicated by black arrow in **Figure 5c**) is found at the edge of the 304SS splat. This morphology can be explained by uneven solidification across the splat. The lower first part contacting with the substrate solidifies rapidly, while the upper parts remain liquid. The momentum of the splat caused the liquid to spread resulting in the wave-like morphology at the edges of splat [29]. Upon impact, a particle

undergoes flattening and solidification in less than 1.5 μs [30]. Then, the particle kinetic energy is partly consumed to overcome viscous resistance and partly converted into viscous energy, surface energy and heat flow. Preheating is beneficial for evaporating adsorbents before deposition. It promotes disk-shaped single splats [29,31].

The morphology of the single splat after 2 min of cavitation erosion is shown in **Figure 5b** and **d**. Some pieces of fragments are delaminated from the periphery of YSZ splat as shown with arrows in **Figure 5b**. The projections around the 304SS and YSZ splats are removed. Moreover, typical cavitation pits are observed on the surface of 304SS splat (see yellow arrows on **Figure 5d**). They indicate the plastic deformation of the surface due to multiple micro-jet surges as shown in [6]. According to Tzanakis *et al.* [32], accumulation of the pits should be considered for the period of time during which destruction of engineering surfaces, such as the splats, occurs. It is obvious that the delamination dominates YSZ (**Figure 5b**) while fragmentation due to cavitation pits initiation as zoomed in red in **Figure 5d** and further cracks formation and growth governs the erosion mechanism in 304SS.

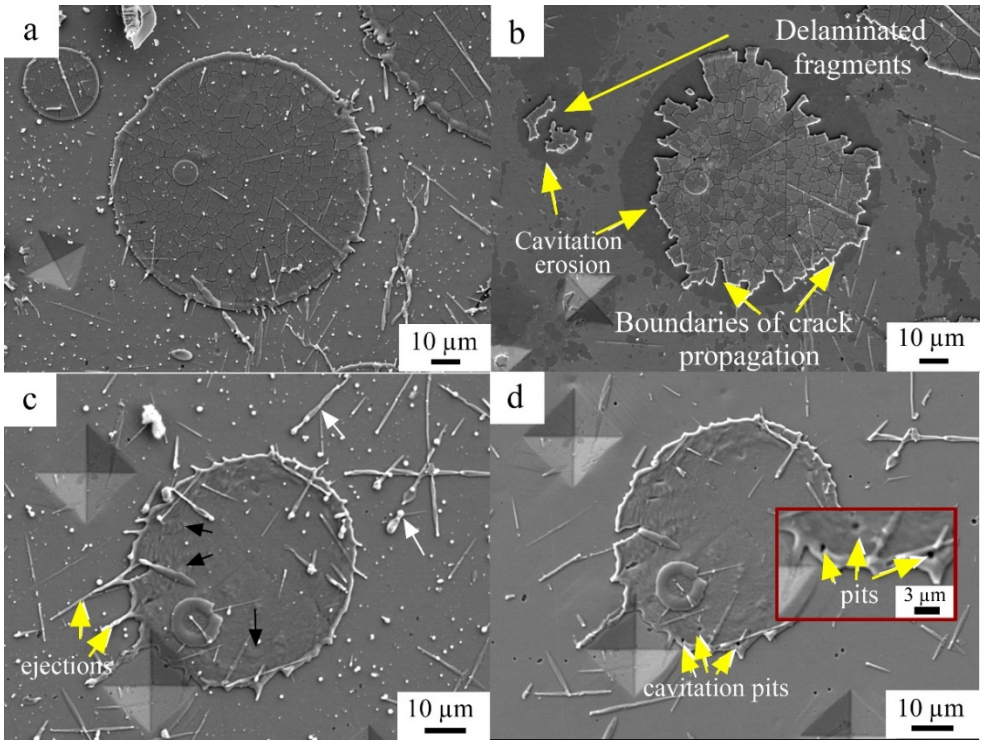

Figure 5: Morphology of single splats for (a) YSZ without cavitation, (b) YSZ after cavitation for 2 min, (c) 304SS without cavitation, and (d) 304SS after cavitation for 2 min

3.3. Stresses exerted by bubble collapsing

During cavitation erosion tests, ultrasound induces a cavitation cloud that consists of numerous bubbles of different sizes. Upon collapsing, bubbles are compressed resulting in high local pressures and temperatures. The centroid moves towards the boundary wall, producing a hollow vortex ring. During the rarefaction phase, the bubble expands and may reach a critical radius, the so-called resonance radius [33]. The bubble then becomes unstable and collapses violently reaching a minimum size. Subsequently, liquid micro-jets followed by powerful shock waves are generated in front of the solid surface and the repeated interaction of these jets and shock-waves with the solid boundary leads to localized degradation of the surface [10]. The bubble cloud exhibits the collective behavior of all these effects with enhanced mechanical interaction with the solid boundary compared with an isolated bubble [34]. The cloud causes more material damage than the collapse of individual bubbles within the cloud. This is because the collapse of a bubble cloud at the

minimum volume concentrates the collapsing energy in the centre of the cloud, therefore, generating extreme local pressure [35]. On the other hand, shielding and scattering effects related to the formation of bubbly clouds significantly disturb the propagation of acoustic waves and the emitted acoustic pressure levels to the liquid media imposing restrictions to cavitation development [36,37] Thus, the effectiveness of bubbly cloud collapse is a trade-off between the aggressiveness of cloud collapses and shielding effects (indicate strong nonlinear bubble dynamics effects). Nevertheless, cavitating bubble clouds are essential for ultrasound material erosion in high intensity sonicated environments [38,39] As the numerical results show in **Figure 6**, high pressures induced by bubble collapse are not spread uniformly everywhere on the surface of specimen, but are concentrated at localized points. This agrees with [40] where severe cavitation was identified in specific areas across the specimen and not across the entire surface. The cavitation impacts start from the periphery of the sample and then, progress towards the center, which agrees well with the experimental findings in **Figure 5**. The mean highest water hammer pressure is up to 1 GPa that agrees well with the numerical predictions of Chahine *et al.* [41]. This pressure is far above the yield stress of materials and produces localized cavitation damages [18,42]. Stronger jet results in higher hammer stresses (**Figure 7**), and this is considered to be the main mechanism for cavitation damage [6]. The water jet from the bubble collapse impinges on the solid surface of the specimen at a velocity around 100-600 m s^{-1} which are of similar order of magnitudes to estimates in the literature [6,43] leading to an instantaneous local hammer pressure of around 0.1-1.0 GPa.

Based on recent reports [44], when metallic systems are subjected to stresses such as cavitation impacts, the main mechanism during the first stage of damage is particle fracture. The stress can reach locally up to 16 GPa for a defect free surface to start plastic deformation. Moreover, areas with defects also require high local stress impacts in the range of 1 GPa. Therefore, and according to [34], it is apparent that a high impact pressure in the range of GPa should be reached

to cause material fracture. This is in good agreement with current results where kinetic energy from jet impingement is partly converted towards the plastic deformation condition of the studied materials (**Figure 8**).

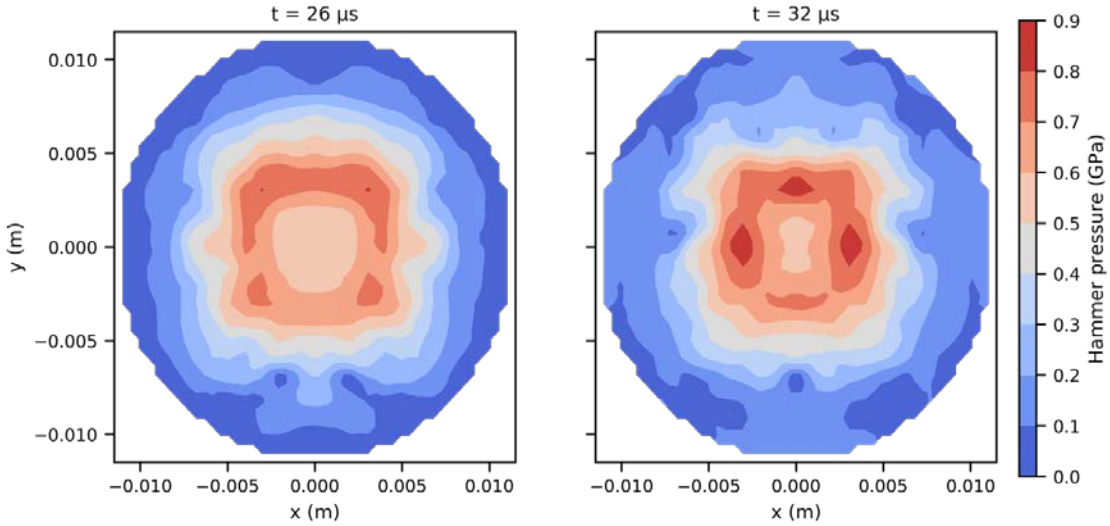

Figure 6: Hammer pressure contour on the surface of specimen at t = 26 µs and t = 32 µs

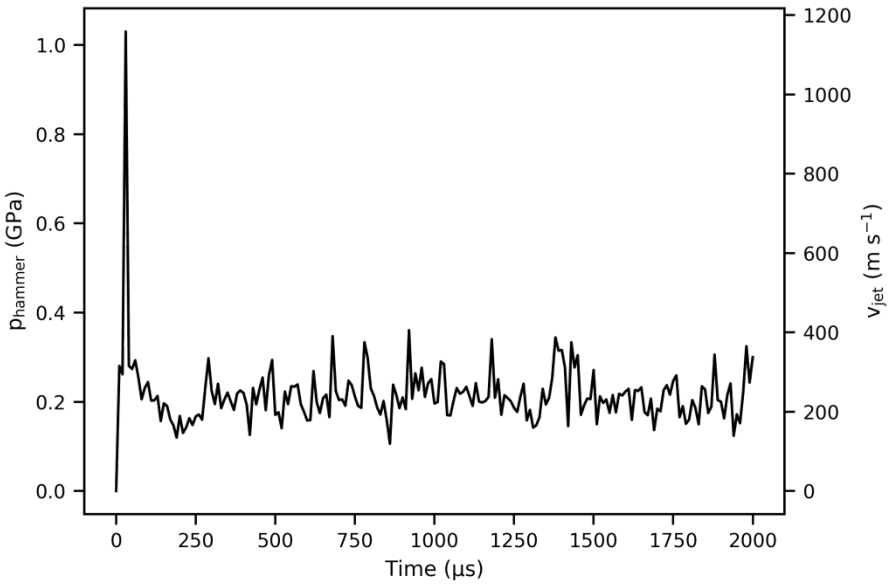

Figure 7: Mean hammer pressure and jet velocity at different cavitation times

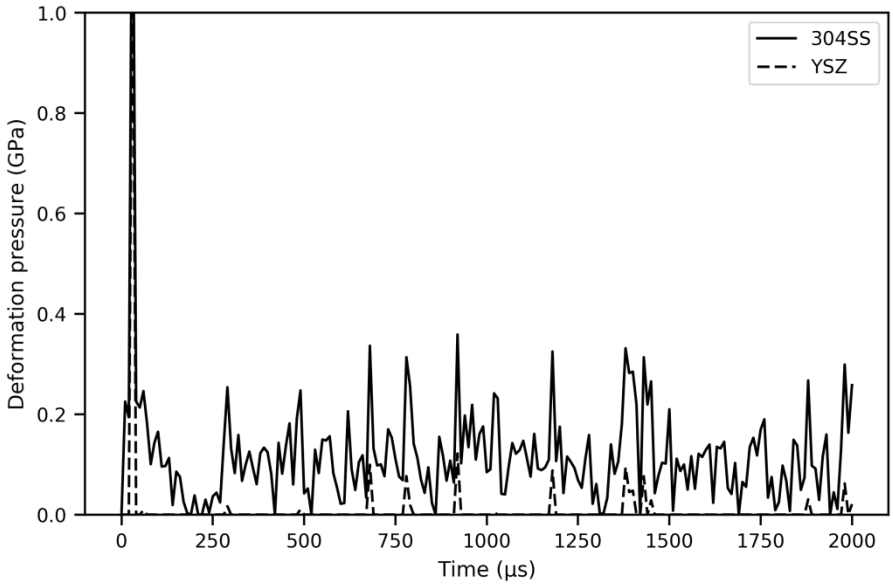

Figure 1: Transient evolution of mean deformation pressures for 304 and YSZ

4. Discussions

4.1. Shear stress during cavitation erosion

Using a sonotrode operating at 20 kHz and with an amplitude of 75 um, Vyas and Preece [45] measured an average compressive stress of 890 MPa in solid surfaces due to cavitation. The stress induced by vapor bubble collapse impacts the solid surface of a single splat from all the directions. Assuming that the stress distribution is uniform across the surface of the splat (P_i = 890 MPa), a 2D single stress on the surface of a splat unit can be described by the equations (8) and (9):

$$\sigma_{x'} = \frac{\sigma_x + \sigma_y}{2} - \frac{\sigma_x - \sigma_y}{2}\cos 2\alpha + \tau_{xy}\sin 2\alpha \qquad (8)$$

$$\tau_{x'y'} = -\frac{\sigma_x - \sigma_y}{2}\sin 2\alpha + \tau_{xy}\cos 2\alpha \qquad (9)$$

where $\sigma_{x'}$ and $\tau_{x'y'}$ represents the normal stress and shear stress in a coordinate system, α is the included angle between axis x′ and x (in the original coordinate system) where in this case was

taken at 45° as the maximum shears stress is of interest as shown in **Figure 9**. The principal normal and shear stresses are calculated using equations (10) and (11):

$$\sigma_{max} = \frac{\sigma_x + \sigma_y}{2} + \sqrt{\left(\frac{\sigma_x - \sigma_y}{2}\right)^2 + {\tau_{xy}}^2} \qquad (10)$$

$$\tau_{max} = \sqrt{\left(\frac{\sigma_x - \sigma_y}{2}\right)^2 + {\tau_{xy}}^2} \qquad (11)$$

With principal stresses being at 1235 MPa and 890 MPa respectively that exceeds the yield stress of most engineering materials. The single splat is fractured and the splat pieces detach due to weak adhesion between the splat and substrate interfaces. For the YSZ splat, the initial network promotes delamination under such value of shear stress.

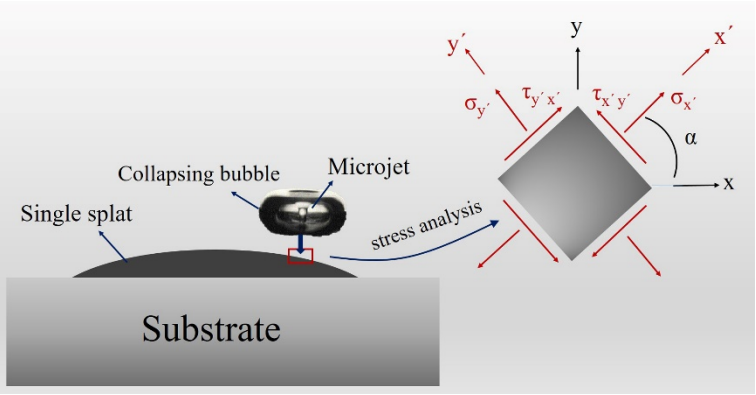

Figure 9: Stress analysis during cavitation erosion

However, cavitation erosion is a time-dependent degradation process initiated by a severe plastic deformation in ductile metals and cracks growth in ceramic materials. Such degradation takes place not only on the surface but also underneath it. The energy released from bubble collapse is transmitted by shock waves several micrometers beyond the surface. The attenuation of acoustic pressure and shock waves during propagation is significant. More than 50% the initial energy was lost by absorption during the first 25 µm of its propagation leading to a modification of the pressure profile during propagation [46]. Similar results were reported by Brujan *et al.* [47], the

pressure was 1.3 ± 0.3 GPa at 68 μm from the bubble wall with the pressure acting on the bubble wall calculated to be as high as 7.7 ± 1.6 GPa. As observed in **Figure 5** and **Figure 6**, large pressure impacts in the center of the specimen do not directly lead to damage. This also explains the time-dependent nature of the cavitation erosion process despite the massive pressures exerted from the bubble collapse as shown by high-speed camera observations in [48]. The first mass loss occurs when both surface and underlying material reach a critical damage condition with cracks large enough to remove the material. Thus, although the calculated stress could exceed the yield strength of most materials on the surface, mass removal does not take place immediately, as was demonstrated for several low resistance metals and alloys [49–51]. These materials also exhibit incubation periods because the underneath layers must undergo cyclic deformation before fracture.

4.2. Cavitation damage of a thermally sprayed coating

Generally, two kinds of coating failures are considered during exposure to cavitation erosion: adhesive and cohesive failures. Adhesion can be understood as the connection between the coating and substrate or between two different splats. On the other hand, the cohesion is commonly referred to the strength forces inside a coating.

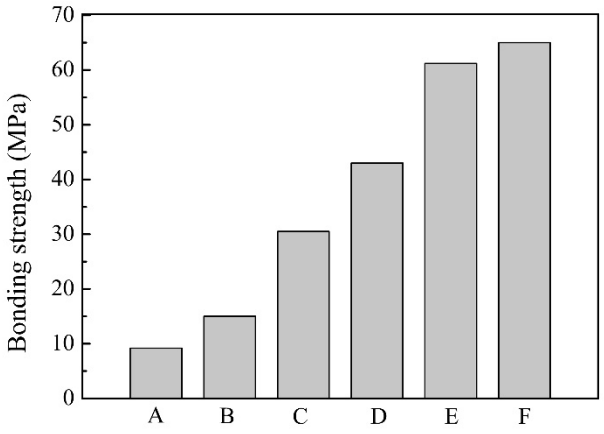

Figure 10: Bonding strength of different thermal sprayed coatings: A [52]: plasma sprayed hydroxyapatite, B [53]: plasma sprayed YSZ, C [54]: plasma sprayed $Ni_{20}Cr$, D [55]: HVOF sprayed Fe-based amorphous composite, E [54]: plasma sprayed $Ni_{20}CrMo$ and F [56] plasma sprayed Al-Si and B_4C composite

If a good adhesion on the surface of a relatively thick coating is obtained, coatings could show a cohesive failure meaning that fragmentation occurs due to cavitation pits initiation and further cracks propagation within the splat as shown in **Figure 5d** and the cumulative erosion-time curve could exhibit an appearance like that produced in bulk materials (case of 304SS). In these cases, microstructural evidence would show a progressive loss of material produced by mechanical degradation because cavitation energy is effectively transmitted into the underlying layers of the coating. Actually, the bonding strength of a thermally sprayed coating is below 100 MPa (see **Figure 10**) demonstrating that the adhesion between dissimilar surfaces with or without different chemical composition, such as adjacent splats in plasma sprayed coatings, is frequently considered as the weakest bonding of the system. Hence, a dominant adhesive failure is expected along with an early detachment of chunks and peripheral ejections as shown in the case of YSZ.

5. Conclusions

The cavitation erosion behaviors of YSZ and 304SS single splats obtained by plasma spraying are studied in this paper. Prior to the cavitation test, in-flight particles temperature and velocity were measured. The mechanism of cavitation erosion of the splats was investigated and discussed using experimental observations and numerical modelling. The main conclusions are summarized as follows:

1. The in-flight particle temperature measurements indicate that 304SS particles are fully molten, while YSZ particles consist of un-melted and half molten particles with a temperature around 2600 °C, which is lower than the melting point of YSZ (~2700 °C). This suggests that the 304SS particles adhere better to the substrate than the YSZ particles.
2. Cavitation induced erosion via detachment of large chunks initiates at the periphery of the YSZ splats and progresses towards the center (i.e. delamination) highlighting adhesive failure. For 304SS splats, fragmentation is caused by cavitation pit initiation, and crack formation and propagation (cohesive failure).
3. Numerical results showed that extreme localized pressures in the range of 1 GPa are induced by bubbles collapsing. These extreme pressures damage the studied surfaces at various locations in due time.

These findings suggest that collapsing cavitation bubbles lead to localized pressures and gradual erosion on the studied splat surfaces. Cavitation damage was in the form of material detachment for YSZ, and pitting, cracks formation for 304SS particles respectively. Mechanical stresses from cavitation impacts and the weak adhesion at the splats interfaces contributes to the early damage of a thermal sprayed coating. Therefore, to improve cavitation resistance, it is crucial to increase the adhesion of individual thermally-sprayed splats by increasing the temperature of the particles during spraying.

Acknowledgements

Yan Wang acknowledges the financial support from China Scholarship Council. Bruno Lebon gratefully acknowledges financial support from EPSRC (UK) under grant number EP/N007638/1. Iakovos Tzanakis gratefully acknowledges financial support from EPSRC (UK) under project UltraMELT 2(EP/R011044/1, EP/R011095/1, EP/R011001/1).

References

[1] J. Stella, E. Schüller, C. Heßing, O.A. Hamed, M. Pohl, D. Stöver, Cavitation erosion of plasma-sprayed NiTi coatings, Wear. 260 (2006) 1020–1027. doi:10.1016/j.wear.2005.06.002.

[2] P.P. Gohil, R.P. Saini, Coalesced effect of cavitation and silt erosion in hydro turbines—A review, Renew. Sustain. Energy Rev. 33 (2014) 280–289. doi:10.1016/j.rser.2014.01.075.

[3] J.R. Laguna-Camacho, R. Lewis, M. Vite-Torres, J.V. Méndez-Méndez, A study of cavitation erosion on engineering materials, Wear. 301 (2013) 467–476. doi:10.1016/j.wear.2012.11.026.

[4] I. Tzanakis, L. Bolzoni, D.G. Eskin, M. Hadfield, Evaluation of Cavitation Erosion Behavior of Commercial Steel Grades Used in the Design of Fluid Machinery, Metall. Mater. Trans. A. 48 (2017) 2193–2206. doi:10.1007/s11661-017-4004-2.

[5] D.G. Shchukin, E. Skorb, V. Belova, H. Möhwald, Ultrasonic cavitation at solid surfaces, Adv. Mater. (2011). doi:10.1002/adma.201004494.

[6] I. Tzanakis, D.G. Eskin, A. Georgoulas, D.K. Fytanidis, Incubation pit analysis and calculation of the hydrodynamic impact pressure from the implosion of an acoustic cavitation bubble, Ultrason. Sonochem. (2014). doi:10.1016/j.ultsonch.2013.10.003.

[7] P. Kumar, R.P. Saini, Study of cavitation in hydro turbines—A review, Renew. Sustain. Energy Rev. 14 (2010) 374–383. doi:10.1016/j.rser.2009.07.024.

[8] R. Singh, S.K. Tiwari, S.K. Mishra, Cavitation Erosion in Hydraulic Turbine Components and Mitigation by Coatings: Current Status and Future Needs, J. Mater. Eng. Perform. 21 (2012) 1539–1551. doi:10.1007/s11665-011-0051-9.

[9] B.K. Sreedhar, S.K. Albert, A.B. Pandit, Improving cavitation erosion resistance of austenitic stainless steel in liquid sodium by hardfacing – comparison of Ni and Co based deposits, Wear. 342 (2015) 92–99. doi:10.1016/j.wear.2015.08.009.

[10] B.K. Sreedhar, S.K. Albert, A.B. Pandit, Cavitation Damage: Theory and Measurements – A Review, Wear. 372 (2016) 177–196. doi:10.1016/j.wear.2016.12.009.

[11] M.K. Padhy, R.P. Saini, A review on silt erosion in hydro turbines, Renew. Sustain. Energy Rev. 12 (2008) 1974–1987. doi:10.1016/j.rser.2007.01.025.

[12] J.F. Santa, J.A. Blanco, J.E. Giraldo, A. Toro, Cavitation erosion of martensitic and austenitic stainless steel welded coatings, Wear. 271 (2011) 1445–1453. doi:10.1016/j.wear.2010.12.081.

[13] A. Kumar, J. Boy, R. Zatorski, L.D. Stephenson, Thermal Spray and Weld Repair Alloys for the Repair of Cavitation Damage in Turbines and Pumps: A Technical Note, (n.d.). doi:10.1361/10599630523737.

[14] M.. Lima, C. Godoy, P.. Modenesi, J.. Avelar-Batista, A. Davison, A. Matthews, Coating fracture toughness determined by Vickers indentation: an important parameter in cavitation erosion resistance of WC–Co thermally sprayed coatings, Surf. Coatings Technol. 177 (2004) 489–496. doi:10.1016/S0257-8972(03)00917-4.

[15] L.M. Yang, A.K. Tieu, D.P. Dunne, S.W. Huang, H.J. Li, D. Wexler, Z.Y. Jiang, Cavitation erosion resistance of NiTi thin films produced by Filtered Arc Deposition, Wear. 267 (2009) 233–243. doi:10.1016/j.wear.2009.01.035.

[16] M. Bitzer, N. Rauhut, G. Mauer, M. Bram, R. Vaßen, H.-P. Buchkremer, D. Stöver, M. Pohl, Cavitation-resistant NiTi coatings produced by low-pressure plasma spraying (LPPS), Wear. 328 (2015) 369–377. doi:10.1016/j.wear.2015.03.003.
[17] J. Stella, T. Poirier, M. Pohl, Cavitation-erosion of 3Y-TZPs obtained at different sintering temperatures, Wear. 300 (2013) 163–168. doi:10.1016/j.wear.2013.01.104.
[18] Y. Wang, G. Darut, T. Poirier, J. Stella, H. Liao, M.-P. Planche, Cavitation erosion of plasma sprayed YSZ coatings produced by feedstocks with different initial sizes, Tribol. Int. 111 (2017). doi:10.1016/j.triboint.2017.03.019.
[19] Z. Wang, A. Kulkarni, S. Deshpande, T. Nakamura, H. Herman, Effects of pores and interfaces on effective properties of plasma sprayed zirconia coatings, Acta Mater. 51 (2003) 5319–5334. doi:10.1016/S1359-6454(03)00390-2.
[20] A. Kulkarni, Z. Wang, T. Nakamura, S. Sampath, A. Goland, H. Herman, J. Allen, J. Ilavsky, G. Long, J. Frahm, R.W. Steinbrech, Comprehensive microstructural characterization and predictive property modeling of plasma-sprayed zirconia coatings, Acta Mater. 51 (2003) 2457–2475. doi:10.1016/S1359-6454(03)00030-2.
[21] G. Mauer, R. Vaßen, D. Stöver, Comparison and Applications of DPV-2000 and Accuraspray-g3 Diagnostic Systems, J. Therm. Spray Technol. 16 (2007) 414–424. doi:10.1007/s11666-007-9047-2.
[22] G.S.B. Lebon, I. Tzanakis, K. Pericleous, D. Eskin, Experimental and numerical investigation of acoustic pressures in different liquids, Ultrason. Sonochem. 42 (2018) 411–421. doi:10.1016/j.ultsonch.2017.12.002.
[23] G.S.B. Lebon, I. Tzanakis, G. Djambazov, K. Pericleous, D.G. Eskin, Numerical modelling of ultrasonic waves in a bubbly Newtonian liquid using a high-order acoustic cavitation model, Ultrason. Sonochem. 37 (2017) 660–668. doi:10.1016/J.ULTSONCH.2017.02.031.
[24] G.L. Chahine, Modeling of Cavitation Dynamics and Interaction with Material, in: 2014: pp. 123–161. doi:10.1007/978-94-017-8539-6_6.
[25] C.-T. Hsiao, A. Jayaprakash, A. Kapahi, J.-K. Choi, G.L. Chahine, Modelling of material pitting from cavitation bubble collapse, J. Fluid Mech. 755 (2014) 142–175. doi:10.1017/jfm.2014.394.
[26] M. Dular, O. Coutier-Delgosha, Numerical modelling of cavitation erosion, Int. J. Numer. Methods Fluids. 61 (2009) 1388–1410. doi:10.1002/fld.2003.
[27] P.A. Lush, Impact of a liquid mass on a perfectly plastic solid, J. Fluid Mech. 135 (1983) 373. doi:10.1017/S0022112083003134.
[28] M. Vardelle, A. Vardelle, P. Fauchais, Spray Parameters and Particle Behavior Relationships During Plasma Spraying, (n.d.).
[29] K. Yang, M. Fukumoto, T. Yasui, M. Yamada, Role of substrate temperature on microstructure formation in plasma-sprayed splats, Surf. Coatings Technol. 214 (2013) 138–143. doi:10.1016/j.surfcoat.2012.11.016.
[30] M. Vardelle, A. Vardelle, A.C. Leger, P. Fauchais, D. Gobin, Influence of particle parameters at impact on splat formation and solidification in plasma spraying processes, J. Therm. Spray Technol. 4 (1995) 50–58. doi:10.1007/BF02648528.
[31] C.-J. Li, J.-L. Li, Evaporated-gas-induced splashing model for splat formation during plasma spraying, Surf. Coatings Technol. 184 (2004) 13–23. doi:10.1016/j.surfcoat.2003.10.048.

[32] I. Tzanakis, M. Hadfield, N. Garland, Cavitation damage incubation with typical fluids applied to a scroll expander system, Tribiology Int. (2011) 1–11. doi:10.1016/j.triboint.2011.06.013.
[33] K. Yasui, Acoustic cavitation and bubble dynamics, Springer, 2018.
[34] E.A. Brujan, T. Ikeda, Y. Matsumoto, Shock wave emission from a cloud of bubbles, Soft Matter. 8 (2012) 5777. doi:10.1039/c2sm25379h.
[35] G.E. REISMAN, Y.-C. WANG, C.E. BRENNEN, Observations of shock waves in cloud cavitation, J. Fluid Mech. 355 (1998) S0022112097007830. doi:10.1017/S0022112097007830.
[36] I. Tzanakis, M. Hodnett, G.S.B. Lebon, N. Dezhkunov, D.G. Eskin, Calibration and performance assessment of an innovative high-temperature cavitometer, Sensors Actuators A Phys. 240 (2016) 57–69. doi:10.1016/j.sna.2016.01.024.
[37] I. Tzanakis, G.S.B. Lebon, D.G. Eskin, K.A. Pericleous, Characterizing the cavitation development and acoustic spectrum in various liquids, Ultrason. Sonochem. 34 (2017) 651–662. doi:10.1016/j.ultsonch.2016.06.034.
[38] Z. Xu, T.L. Hall, J.B. Fowlkes, C.A. Cain, Optical and acoustic monitoring of bubble cloud dynamics at a tissue-fluid interface in ultrasound tissue erosion, J. Acoust. Soc. Am. 121 (2007) 2421–2430. doi:10.1121/1.2710079.
[39] J. Ma, C.-T. Hsiao, G.L. Chahine, Numerical study of acoustically driven bubble cloud dynamics near a rigid wall, Ultrason. - Sonochemistry. 40 (2017) 944–954. doi:10.1016/j.ultsonch.2017.08.033.
[40] G.G.-A. Fatjó, A. Torres Pérez, M. Hadfield, Experimental study and analytical model of the cavitation ring region with small diameter ultrasonic horn, Ultrason. Sonochem. 18 (2011) 73–79. doi:10.1016/J.ULTSONCH.2009.12.006.
[41] G.L. CHAHINE, PRESSURES GENERATED BY A BUBBLE CLOUD COLLAPSE, Chem. Eng. Commun. 28 (1984) 355–367. doi:10.1080/00986448408940143.
[42] Y. Wang, J. Stella, G. Darut, T. Poirier, H. Liao, M.-P. Planche, APS prepared NiCrBSi-YSZ composite coatings for protection against cavitation erosion, J. Alloys Compd. (2017). doi:10.1016/j.jallcom.2017.01.034.
[43] O. Supponen, D. Obreschkow, P. Kobel, M. Farhat, Luminescence from cavitation bubbles deformed in uniform pressure gradients, Phys. Rev. E. 96 (2017). doi:10.1103/PhysRevE.96.033114.
[44] M.G. Mueller, G. Žagar, A. Mortensen, In-situ strength of individual silicon particles within an aluminium casting alloy, Acta Mater. 143 (2018) 67–76. doi:10.1016/J.ACTAMAT.2017.09.058.
[45] B. Vyas, C.M. Preece, Stress produced in a solid by cavitation, J. Appl. Phys. 47 (1976) 5133–5138. doi:10.1063/1.322584.
[46] R. Pecha, B. Gompf, Microimplosions: Cavitation Collapse and Shock Wave Emission on a Nanosecond Time Scale, Phys. Rev. Lett. 84 (2000) 1328–1330. doi:10.1103/PhysRevLett.84.1328.
[47] E.A. Brujan, T. Ikeda, Y. Matsumoto, On the pressure of cavitation bubbles, Exp. Therm. Fluid Sci. 32 (2008) 1188–1191. doi:10.1016/J.EXPTHERMFLUSCI.2008.01.006.
[48] F. Wang, I. Tzanakis, D. Eskin, J. Mi, T. Connolley, Ultrasonics - Sonochemistry In situ observation of ultrasonic cavitation-induced fragmentation of the primary crystals formed in Al alloys (a) (b), Ultrason. - Sonochemistry. 39 (2017) 66–76. doi:10.1016/j.ultsonch.2017.03.057.

[49] A. Krella, An experimental parameter of cavitation erosion resistance for TiN coatings, Wear. 270 (2011) 252–257. doi:10.1016/j.wear.2010.10.065.
[50] A. Krella, Cavitation erosion of TiN and CrN coatings deposited on different substrates, Wear. 297 (2013) 992–997. doi:10.1016/j.wear.2012.11.049.
[51] C. Haosheng, L. Jiang, C. Darong, W. Jiadao, Damages on steel surface at the incubation stage of the vibration cavitation erosion in water, Wear. 265 (2008) 692–698. doi:10.1016/j.wear.2007.12.011.
[52] Y.C. Yang, E. Chang, Influence of residual stress on bonding strength and fracture of plasma-sprayed hydroxyapatite coatings on Ti–6Al–4V substrate, Biomaterials. 22 (2001) 1827–1836. doi:10.1016/S0142-9612(00)00364-1.
[53] R. C.S., B. V., A. P.V., V. V., Influence of the intermixed interfacial layers on the thermal cycling behaviour of atmospheric plasma sprayed lanthanum zirconate based coatings, Ceram. Int. 38 (2012) 4081–4096. doi:10.1016/j.ceramint.2012.01.066.
[54] J.-J. Tian, S.-W. Yao, X.-T. Luo, C.-X. Li, C.-J. Li, An effective approach for creating metallurgical self-bonding in plasma-spraying of NiCr-Mo coating by designing shell-core-structured powders, Acta Mater. 110 (2016) 19–30. doi:10.1016/j.actamat.2016.03.020.
[55] C. Zhang, H. Zhou, L. Liu, Laminar Fe-based amorphous composite coatings with enhanced bonding strength and impact resistance, Acta Mater. 72 (2014) 239–251. doi:10.1016/j.actamat.2014.03.047.
[56] O. Sarikaya, E. Celik, S.C. Okumus, S. Aslanlar, S. Anik, Effect on residual stresses in plasma sprayed Al–Si/B4C composite coatings subjected to thermal shock, Surf. Coatings Technol. 200 (2005) 2497–2503. doi:10.1016/j.surfcoat.2004.08.071.